Bio-Design and Manufacturing (2026) 9:165–181
https://doi.org/10.1631/bdm.2500298

RESEARCH ARTICLE

Bonding heterostructure mediated "photo-thermo-electric" implant: NIR-II photothermal and thermoelectric therapy for bone tumor defects

Jun Zan[1,2] · Jiachi Zhao[2] · Jie Zeng[2] · Qian Yang[3] · Hengyun Ye[4] · Youwen Yang[2] · Cijun Shuai[1,2,5]

Received: 10 June 2025 / Accepted: 24 September 2025

Abstract

Recurrence of solid tumors after surgical resection is a major barrier to tissue regeneration. As an emerging treatment strategy, photo-thermo-electric therapy ablates tumor cells via photothermal effects and generates reactive oxygen species (ROS) via thermoelectric effects to disrupt heat shock proteins, thereby suppressing their protective function in tumor cells. However, conventional materials suffer from low thermoelectric efficiency and weak tissue penetration ability. In this study, we fabricated iodine-doped bismuth sulfide (I-Bi_2S_3) nanorods with bonding heterostructures to improve thermoelectric performance. The approach employed iodine doping to introduce additional electrons, thereby regulating the band structure of Bi_2S_3 and exploiting the dual low-energy vibration effect of the heterostructures to reduce thermal conductivity. More importantly, controlling the type of heterostructure modulated the bandgap width, thereby expanding the light absorption range to the higher-penetration near-infrared (NIR)-II region for deep tissue treatment. The I-Bi_2S_3 nanorods were incorporated into poly-L-lactic acid (PLLA) scaffolds to confer antitumor functionality. According to the results, the bonding heterostructures enhanced the conductivity of Bi_2S_3 and reduced its thermal conductivity, significantly enhancing thermoelectric efficacy. The heterostructures reduced the bandgap of Bi_2S_3 from 1.23 to 0.88 eV, enabling optical absorption in the NIR-II region. The ROS tests showed that the PLLA/I-Bi_2S_3 scaffold exhibited good photothermal effects and ROS generation under 1064-nm laser irradiation. The antitumor efficacy of the PLLA/I-Bi_2S_3 scaffold reached 84.6% against MG-63 cells, demonstrating its exceptional potential in cancer treatment.

Jun Zan and Jiachi Zhao have contributed equally to this work.

✉ Youwen Yang
yangyouwen@jxust.edu.cn

✉ Cijun Shuai
shuai@csu.edu.cn

[1] School of Sino-German Robotics, Shenzhen University of Information Technology, Shenzhen 518172, China

[2] Jiangxi Provincial Key Laboratory of Additive Manufacturing of Implantable Medical Device, Jiangxi University of Science and Technology, Nanchang 330013, China

[3] Department of Radiation and Medical Oncology, Zhongnan Hospital of Wuhan University, Wuhan 430072, China

[4] Chaotic Matter Science Research Center, Jiangxi University of Science and Technology, Ganzhou 341000, China

[5] State Key Laboratory of Precision Manufacturing for Extreme Service Performance, College of Mechanical and Electrical Engineering, Central South University, Changsha 410083, China

Graphical abstract

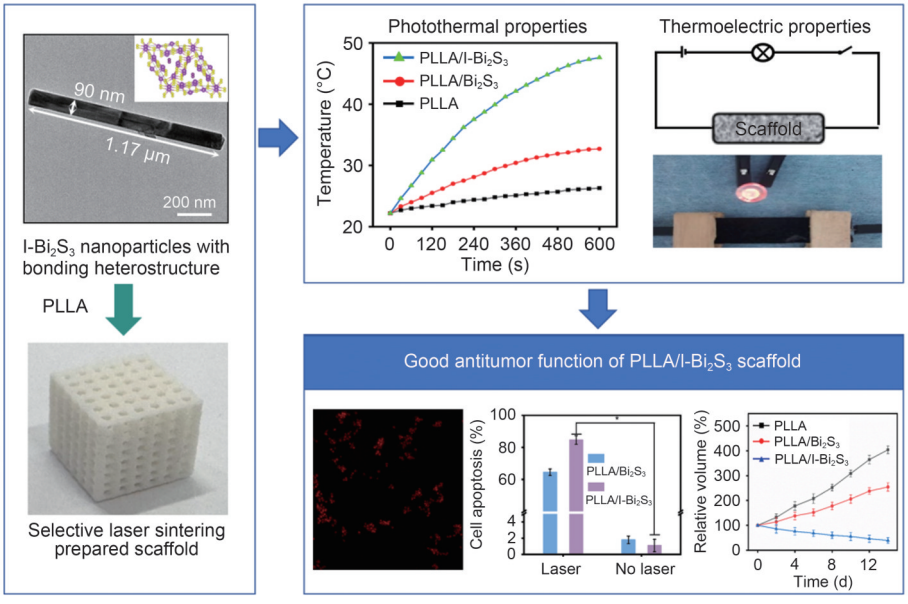

Keywords Antitumor bone scaffolds · Photo-thermo-electric therapy · Near-infrared II window · Bonding heterostructures · Selective laser sintering

1 Introduction

Tumor-induced tissue defects have long posed a major challenge for the medical community, particularly osteosarcoma, which primarily occurs in children and adolescents [1, 2]. On the one hand, surgical resection rarely removes malignant tumor tissue completely; thus, recurrent tumor cells quickly invade healthy bone tissue and even newly formed bone tissue [3, 4]. On the other hand, the defective tissue after surgical resection is difficult to repair by self-healing [5]. Recently, the development of degradable implants with antitumor functions using three-dimensional (3D) printing has emerged as a promising treatment approach [6, 7]. Specifically, 3D-printed biodegradable scaffolds (such as poly-L-lactide (PLLA) and poly(lactic-co-glycolic acid)) not only precisely match the host bone defect to realize sufficient mechanical support but also serve as growth sites to promote cell adhesion and growth [8–10]. Importantly, scaffolds with antitumor functions can prevent tumor recurrence and provide a suitable growth environment for tissue regeneration [11].

Currently, the primary methods for endowing implants with antitumor capabilities include chemotherapy, photothermal therapy (PTT), and photodynamic therapy (PDT) [12]. Chemotherapy typically faces limitations due to drug resistance, low treatment efficacy, and side effects [13]. In contrast, PTT and PDT offer benefits such as noninvasiveness, broad therapeutic ranges, and low resistance [14, 15]. However, the overexpression of heat shock proteins (HSPs) in tumor cells can diminish PTT effectiveness, and the reactive oxygen species (ROS) generated by PDT have a short duration of action [16, 17]. Photo-thermo-electric therapy has recently emerged as a promising strategy for cancer treatment, combining the strengths of PTT and PDT [18]. In this approach, PTT is first used to generate localized high temperatures to ablate tumor cells, while pyroelectric therapy leverages the temperature differences to produce ROS, which disrupt HSPs, thereby enhancing antitumor efficacy.

Bismuth sulfide (Bi_2S_3), a typical photo-thermo-electric material, has attracted considerable attention for its good biocompatibility, narrow bandgap, and good light absorption [19]. However, its low thermoelectric efficiency at normal temperatures and weak tissue penetration restrict its application in bone tissue [20]. Research has shown that inserting a third phase into binary compounds can significantly modify the electronic and phonon structures, thereby enhancing their thermoelectric performance. Constructing bonding heterogeneity to improve the overall performance is an effective strategy [21]. For example, introducing halogen elements (such as iodine, chlorine, and bromine) into Bi_2S_3 is expected to form bonding heterostructures. Iodine

exhibits high electronegativity and strong polarizability; thus, the doping of iodine (I) atoms into the Bi_2S_3 structure will partially substitute sulfur atoms and modulate the coordination environment of Bi via ionic polarization effects, thereby inducing the formation of Bi^{2+}–Bi^{2+} covalent bonds [22, 23]. In this case, covalent bonds such as Bi–S, Bi–I, and Bi–Bi rearrange within the lattice to form a bonded heterogeneous crystal cell structure (e.g., $Bi_{13}S_{18}I_2$ or $Bi_{19}S_{27}I_3$). The additional electrons introduced by iodine doping can regulate the band structure, thereby increasing the carrier concentration and enhancing electrical conductivity [24, 25]. In addition, the iodine atoms and subvalent dimers introduce dual low-energy vibrations, which reduce lattice thermal conductivity, thereby improving thermoelectric conversion efficiency. Moreover, the bonded heterogeneous structure forms with good interfacial compatibility, avoiding the interface resistance caused by lattice mismatch and further enhancing thermoelectric stability.

More importantly, this process also holds promise for extending the light absorption range of Bi_2S_3 into the near-infrared (NIR)-II region with deep penetration, thereby enabling photothermal responsiveness in deep bone tissue environments (>3 cm). This is because iodine doping and the formation of bonded heterogeneous structures reconstruct the Bi_2S_3 band structure, introducing new donor levels between the valence band (VB) and conduction band (CB) and significantly narrowing the bandgap. If the doping process can be precisely tuned to achieve a bandgap width within the range of 0.73–1.24 eV, electrons can be excited by lower-energy photons corresponding to the NIR-II region, enabling photothermal conversion under NIR-II irradiation [26, 27]. Additionally, the presence of multiple bonding states within the heterostructure may cause local polarity variations, thereby generating weak built-in electric fields within the material. These fields facilitate the separation of photogenerated electron–hole pairs, further improving photothermal conversion efficiency.

In this study, iodine-doped Bi_2S_3 (I-Bi_2S_3) nanoparticles (NPs) with $Bi_{13}S_{18}I_2$ and $Bi_{19}S_{27}I_3$ heterostructures were first synthesized using a hydrothermal reaction method to fabricate a functional NP with enhanced photothermal–thermoelectric properties. The resulting I-Bi_2S_3 NPs were then incorporated into PLLA scaffolds using laser 3D printing technology for antitumor therapy. The morphology and phase composition of the synthesized I-Bi_2S_3 NPs were comprehensively analyzed. The functional characteristics of the PLLA/I-Bi_2S_3 scaffolds were investigated, including photothermal and thermoelectric performance and the corresponding ROS generation ability. The antitumor function of the scaffold was detected through cell and animal experiments. Furthermore, the antitumor mechanism was studied in detail. This study proposes an antitumor scaffold based on photothermal–thermoelectric therapy, providing a therapeutic approach for tissue regeneration following osteosarcoma resection.

2 Experimental section

2.1 Material source and synthesis

2.1.1 Material source

PLLA powder (M_w=1.5×10^4 Da, melting point of approximately 175 °C) was obtained from Polymtek Biomaterial Co., Ltd. (Shenzhen, China). Bismuth nitrate pentahydrate ($Bi(NO_3)_3 \cdot 5H_2O$, 99%), thiourea ($CS(NH_2)_2$, 99%), and potassium iodide (KI, 99%) were purchased from Aladdin Biological Co., Ltd. (Shanghai, China).

2.1.2 Synthesis of I-Bi_2S_3

I-Bi_2S_3 was synthesized using a hydrothermal reaction method. In detail, 0.1 mmol/L of $Bi(NO_3)_3 \cdot 5H_2O$ was dissolved in 30 mL of deionized water and stirred for 2 h to ensure complete dissolution. Next, 38 mg of $CS(NH_2)_2$ and 0.2 mg of KI were added, and the mixture was stirred for an additional 30 min. The resulting solution was transferred into a 50-mL Teflon-lined autoclave and heated at 200 °C for 8 h. After cooling, the black precipitate (I-Bi_2S_3 powder) was washed, centrifuged with deionized water, and dried in a vacuum oven. For comparison, Bi_2S_3 powder was synthesized under identical conditions, excluding the addition of KI.

2.2 Characterization

The micro-morphology of the I-Bi_2S_3 NPs was observed using transmission electron microscopy (TEM; Tecnai F20, FEI, USA). The elemental composition of the I-Bi_2S_3 NPs was examined using energy-dispersive X-ray spectroscopy (EDS). The phase structure and surface chemical composition were investigated using X-ray diffraction (XRD; Empyrean, the Netherlands) and X-ray photoelectron spectroscopy (XPS; Thermo-VG Scientific Ltd., UK), respectively. Electrochemical properties were evaluated using an electrochemical workstation (CHI660E, China) with a standard three-electrode setup, where Ag/AgCl, platinum foil, and the sample served as the reference, counter, and working electrodes, respectively. Electrochemical impedance spectroscopy (EIS) and Mott–Schottky analyses were performed using a 2.5-mmol/L potassium ferricyanide solution, and photocurrent measurements were performed using a 0.5-mol/L Na_2SO_4 solution. EIS data were collected across a frequency range of 100 kHz–0.1 Hz with an amplitude of 0.5 V [28, 29]. Ultraviolet–visible (UV–Vis) absorption and diffuse reflectance spectra were recorded using a UV-2700 spectrophotometer (Shimadzu, China).

To elucidate the changes in the energy band structure and density of states (DOS) after the iodine doping of Bi_2S_3, first-principles calculations were performed using the Cambridge Sequential Total Energy Package simulation program based on density functional theory (DFT). The Perdew–Burke–Ernzerhof exchange–correlation functional within the generalized gradient approximation was used [30–32]. The electronic plane-wave cutoff energy was set to 350 eV, and all structures were optimized until the energy differences converged to $<10^{-4}$ eV and the atomic forces fell below 0.01 eV/Å (1 Å=1×10^{-10} m). In detail, an orthorhombic Bi_2S_3 unit cell (a=11.593 59 Å, b=3.997 99 Å, c=11.160 62 Å) with k-point meshes of 1×3×1 was used in the initial calculations (Bi atoms: 8; S atoms: 12). To investigate the impact of iodine incorporation, the I-Bi_2S_3 structure was modeled using a $Bi_{13}S_{18}I_2$ unit cell with a 6% iodine content. This model featured k-point meshes of 1×1×2 and a supercell with a doubled z-axis to account for disordered Bi atoms (Bi atoms: 26; S atoms: 36; I atoms: 4). The convergence conditions were consistent with those used for Bi_2S_3 optimization. The energy band structure of the optimized cells was calculated, and the total DOS (TDOS) and the projected DOS (PDOS) were analyzed to investigate the electronic structural variations induced by iodine doping.

2.3 Preparation and performance testing of scaffolds

PLLA/I-Bi_2S_3 scaffolds were fabricated using a custom-built selective laser sintering (SLS) system. The mass ratio of PLLA to I-Bi_2S_3 powder was 98:2. The sintering parameters were as follows: a scan speed of 100 mm/s at a laser power of 0.6 W and a scan speed of 200 mm/s at a laser power of 0.8 W. A layer thickness of 0.1 mm was maintained during fabrication. Scaffolds measuring 15 mm× 5 mm×1.5 mm were fabricated for the mechanical and electrical tests, whereas smaller scaffolds (Φ4 mm×1.5 mm) were used in the biological experiments. The electrical conductivity of the scaffolds was tested using a three-electrode system, confirming their suitability for conductive applications. The photothermal performance of the scaffolds, including time–temperature curves and photothermal stability, was investigated under 1064-nm laser irradiation at 1.5 W/cm^2.

2.4 ROS analysis of scaffolds

To investigate thermally induced active radical generation, electron spin resonance (ESR) testing was conducted using 5,5-dimethyl-1-pyrroline N-oxide (DMPO) as a radical capture agent. The ESR spectra were recorded under 1064-nm irradiation to identify various ROS, including hydroxyl radicals (·OH) and singlet oxygen ($^1O_2$). DMPO (100 mmol/L) was used to detect ·OH, whereas 2,2,6,6-tetramethylpiperidine-1-oxyl (TEMP, 100 mmol/L) was used to capture $^1O_2$. To further quantify ROS generation, 1,3-diphenylisobenzofuran (DPBF) was used to detect the $^1O_2$ levels via UV–Vis spectroscopy. Similarly, 3,3',5,5'-tetramethylbenzidine (TMB) and O-phenylenediamine (OPD) were used to measure the ·OH levels.

2.5 Antitumor performance of scaffolds

2.5.1 Live/Dead staining assays

The MG-63 human osteosarcoma cell line was incubated in a complete cell culture medium containing 10% fetal bovine serum and 1% penicillin–streptomycin. The cells were cultured in Dulbecco's modified Eagle's medium and maintained at 37 °C under 5% CO_2 atmosphere and 95% humidity. MG-63 cells were seeded into six-well plates at a density of 5×10^5 per well and incubated overnight under standard culture conditions. Subsequently, the PLLA, PLLA/Bi_2S_3, and PLLA/I-Bi_2S_3 scaffolds were added after the cells adhered to the wall. For the laser-treated group, the cells were irradiated with a 1064-nm laser (1.5 W/cm^2) until the temperature reached 45 °C, followed by 5 min of irradiation. After an additional 24 h of co-culture, the cells were stained with calcein acetoxymethyl ester/propidium iodide (Calcein-AM/PI) and Hoechst 33342. The staining process involved removing the culture medium and the scaffolds, washing the cells three times with phosphate-buffered saline (PBS), and adding a 500-μL Hoechst 33342 working solution (0.5 μg) containing a 0.5-μL Calcein-AM solution (2 mmol/L) and a 1.5-μL PI solution (1.5 mmol/L). The cells were incubated at 37 °C in the dark for 30 min and then visualized using a fluorescence microscope.

2.5.2 Cell counting kit-8 assays and cell adhesion

The MG-63 cells were plated in a 96-well plate at a density of 5×10^3 per well and incubated overnight. Subsequently, the scaffolds were introduced [33]. The cells were irradiated daily with a 1064-nm laser (1.5 W/cm^2) until the temperature reached 45 °C, followed by 5 min of irradiation. After 24 h of additional co-culture, cell viability was assessed using a cell counting kit-8 (CCK-8) assay. In addition, the cell adhesion was observed using scanning electron microscopy (SEM) after 5 d of culture.

2.5.3 ROS staining assays

After scaffold addition and co-culture for 24 h, the cells in the laser-treated group were irradiated with a 1064-nm laser (1.5 W/cm^2) until the temperature reached 45 °C, followed by 5 min of irradiation. The cells were then stained with 2',7'-dichlorodihydrofluorescein diacetate (DCFH-DA) to

detect ROS. After removing the medium and the scaffolds, the cells were washed three times with PBS, and 500 μL of a DCFH-DA solution (1 μmol/L) was added. The cells were incubated at 37 °C in the dark for 30 min and observed using a fluorescence microscope.

2.5.4 HSP assays

Intracellular HSP90 expression was evaluated using Western blotting. MG-63 cells were seeded in six-well plates at a density of 5×10^4 cells/well. After co-culturing the cells and scaffolds, they were subjected to three cycles of heating in a water bath at 37–45 °C, followed by cell lysis. The protein concentration was determined using a protein quantification kit (Beyotime, China). The protein samples were separated by sodium dodecyl sulfate–polyacrylamide gel electrophoresis, transferred to polyvinylidene fluoride membranes, and blocked with 5% bovine serum albumin at 37 °C overnight. The membranes were incubated with primary antibodies overnight and then with secondary antibodies for 1 h at room temperature. The signals were detected using electrochemiluminescence and imaged using a gel imager.

2.5.5 Necrosis and apoptosis detection

To analyze cell death, the MG-63 cells were seeded in six-well plates and co-cultured with the scaffolds. After laser irradiation (as described above), the cells were harvested and washed three times after three days. Annexin V-FITC (5 μL) and PI (10 μL) staining solutions were added to the cells; the mixtures were gently mixed and incubated at room temperature in the dark for 15 min. Finally, the samples were analyzed using flow cytometry to distinguish between the necrotic and apoptotic cells.

2.6 In vivo antitumor experiment of scaffolds

Eighteen female nude mice (4–6 weeks old) were used to establish a subcutaneous osteosarcoma model. After one week of adaptive feeding, human osteosarcoma MG-63 cells were digested with trypsin and resuspended at 1×10^7 cells/mL, and 0.5 mL of the suspension was subcutaneously injected into the dorsal region of each mouse. When the tumor volume reached approximately 100 mm^3, the animals were randomly divided into three groups, namely, PLLA, PLLA/Bi_2S_3, and PLLA/I-Bi_2S_3, based on the type of scaffold implanted and their exposure to NIR-II irradiation [34].

The surgical procedure involved anesthesia and disinfection, consistent with standard protocols. The tumor mass was exposed by making an incision along its long axis, and bleeding was controlled using a gauze. A cylindrical scaffold (Φ4 mm×1.5 mm) was implanted into the center of the tumor tissue, and the incisions were closed layer by layer with sutures. Post-surgical care included disinfection with complex iodine and intramuscular penicillin injections to prevent infection, followed by daily oral penicillin administration for three consecutive days. Two days after surgery, NIR-II laser irradiation (1064 nm, 1.5 W/cm^2) was applied at the tumor site, with the tumor surface temperature monitored in real time using an infrared thermal imaging system (FLIR, Teledyne FLIR Systems, USA). The first irradiation was defined as Day 0, and this timeline was used for all subsequent daily irradiations. The tumor volume was calculated as follows:

$$V_{\text{tumor}}=(L_{\text{tumor}}\times W_{\text{tumor}})^2/2-V_{\text{scaffold}},$$

where V_{tumor}, L_{tumor}, W_{tumor}, and V_{scaffold} represent the tumor volume, tumor length, tumor width, and scaffold volume (19 mm^3), respectively. On Day 14, all mice were sacrificed. The tumor tissues were harvested, fixed in 4% paraformaldehyde, embedded in paraffin, and sectioned for hematoxylin and eosin (H&E) staining. The H&E staining procedure followed standard protocols. In addition, apoptosis in the osteosarcoma tissues was assessed using the terminal deoxynucleotidyl transferase dUTP nick end labeling (TUNEL) assay.

2.7 Statistical analysis

Data are presented as mean±standard deviation ($n\geq3$). The odds ratios and 95% confidence intervals were calculated, and two-tailed tests were conducted to assess statistical significance. A p-value of ≤0.05 was considered significant.

3 Results and discussion

3.1 Microstructure analysis of I-Bi_2S_3

The morphology of the I-Bi_2S_3 powder was characterized using TEM (Fig. 1). The I-Bi_2S_3 powder exhibited a typical nanorod-like structure, with an axial length ranging from 0.7 to 1.2 μm based on statistical analysis (Figs. 1a and 1b). According to the EDS elemental mapping analysis, Bi, S, and I were evenly distributed in the entire structure (Fig. 1c), demonstrating the successful synthesis of I-Bi_2S_3. As shown in Fig. 1d, the crystal structure of I-Bi_2S_3 exhibited the same diffraction peaks as those of Bi_2S_3 (at 24.9°, 28.6°, and 31.8°), corresponding to the (130), (121), and (221) lattice planes, respectively. The two new diffraction peaks at 23.7° and 28.2° correspond to the (130) and (121) planes of the $Bi_{19}S_{27}I_3$ crystal. The selected area electron diffraction (SAED) images of I-Bi_2S_3 (Fig. 1e) further proved that the identical diffraction crystal planes were

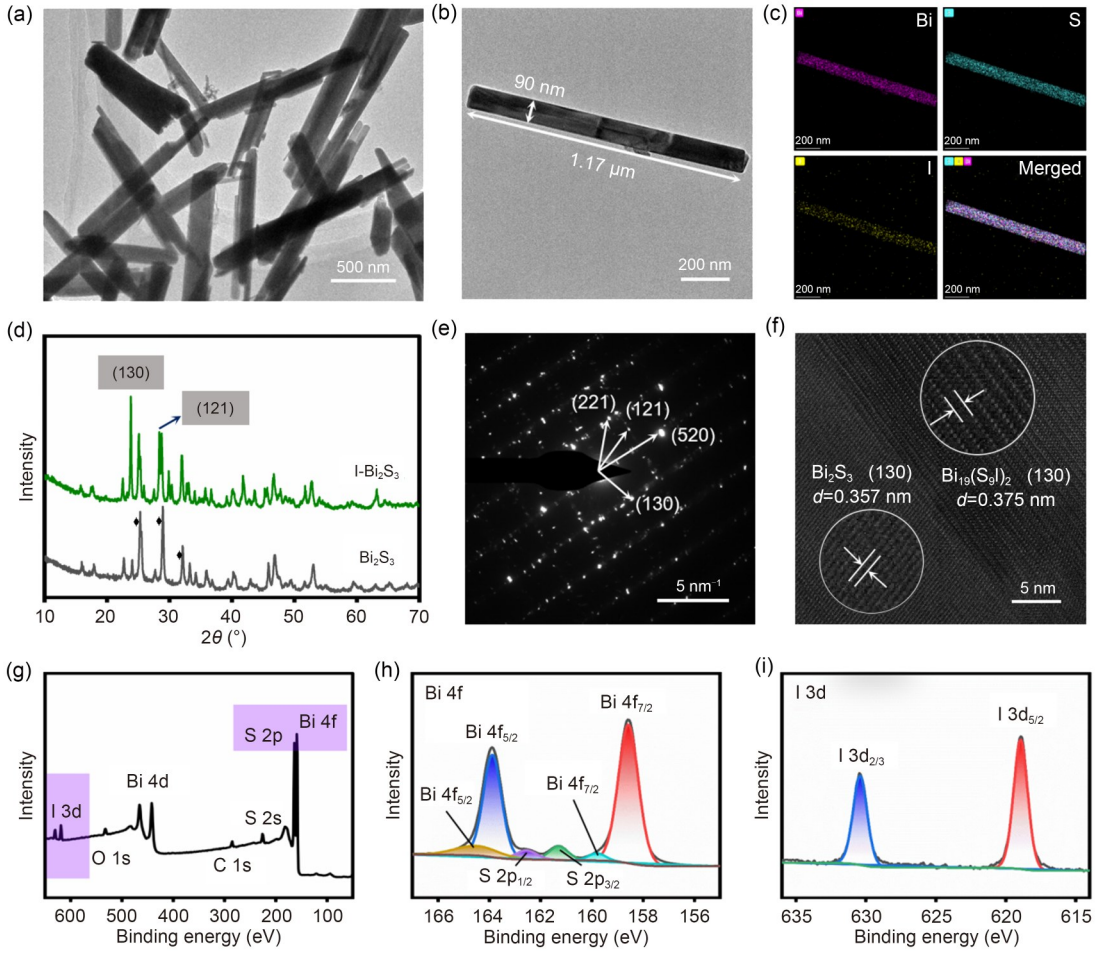

Fig. 1 Microstructure analysis of I-Bi_2S_3. TEM images (a, b) and elemental mappings (c) of I-Bi_2S_3 nanorods. XRD pattern (d), SAED pattern (e), and lattice fringes (f) of I-Bi_2S_3 powder. (g–i) Wide-survey XPS spectrum and Bi 4f and I 3d spectra of I-Bi_2S_3

consistent with those of the (221), (121), and (520) planes of previously reported $Bi_{19}S_{27}I_3$ crystals [35]. The crystal plane spacing of I-Bi_2S_3 was measured using local Fourier transform. The interplanar spacings of 0.357 and 0.375 nm matched well with the (130) plane of Bi_2S_3 and the (130) crystal plane of $Bi_{13}S_{18}I_2$, respectively (Fig. 1f). These results demonstrated that iodine doping induced the formation of $Bi_{19}S_{27}I_3$ and $Bi_{13}S_{18}I_2$ heterostructures within the I-Bi_2S_3 nanorods.

The XPS spectrum of I-Bi_2S_3 was characterized to analyze the interaction between I atoms and Bi_2S_3. As shown in Fig. 1g, the elemental composition comprised Bi, I, and S, and the chemical states were I 3d, Bi 4d, S 2s, S 2p, and Bi 4f in the entire spectrum. The high-resolution Bi 4f XPS peaks at 158.6 and 163.8 eV were attributed to Bi $4f_{7/2}$ and Bi $4f_{5/2}$, respectively, confirming the formation of Bi–I and Bi–S bonds (Fig. 1h). The different binding energies may account for the existence of bivalent Bi (II) in I-Bi_2S_3 [36]. Furthermore, the I 3d spectrum comprised two peaks at 618.8 and 630.4 eV, corresponding to I $3d_{5/2}$ and I $3d_{3/2}$, respectively [37] (Fig. 1i).

In summary, we successfully synthesized the target I-Bi_2S_3 nanorods through a one-step hydrothermal reaction (Fig. 2a). The successful iodine doping was confirmed by EDS mapping, which also revealed the phase composition and corresponding chemical state of I-Bi_2S_3. Notably, the incorporation of I atoms affected the original Bi_2S_3 crystal structure, resulting in the formation of a new phase. This reconstruction, primarily driven by iodine doping, resulted in a $Bi_{13}S_{18}I_2$ structure with bivalent Bi (II) [38]. Moreover, to the best of our knowledge, bivalent Bi (II) acts as Bi_2^{4+} dimers in I-Bi_2S_3. To verify this hypothesis, the band structure and DOS distribution of I-Bi_2S_3 were investigated using DFT calculations. As shown in Figs. 2b–2d, an optimized Bi_2S_3 unit cell (a=11.941 506 Å, b=4.027 079 Å, and c=11.164 037 Å) was used as an indirect semiconductor, exhibiting a band gap of 1.291 eV. This value is consistent with the optical measurements reported by Groom et al. [39]. For the optimized $Bi_{13}S_{18}I_2$ unit cell, its lattice constant was a=15.612 Å, b=15.612 Å, and c=8.0336 Å, and the stable atomic coordinates of I atoms in the crystal cell were (0.333 33, 0.666 67, 0.374 98) and (−0.333 33,

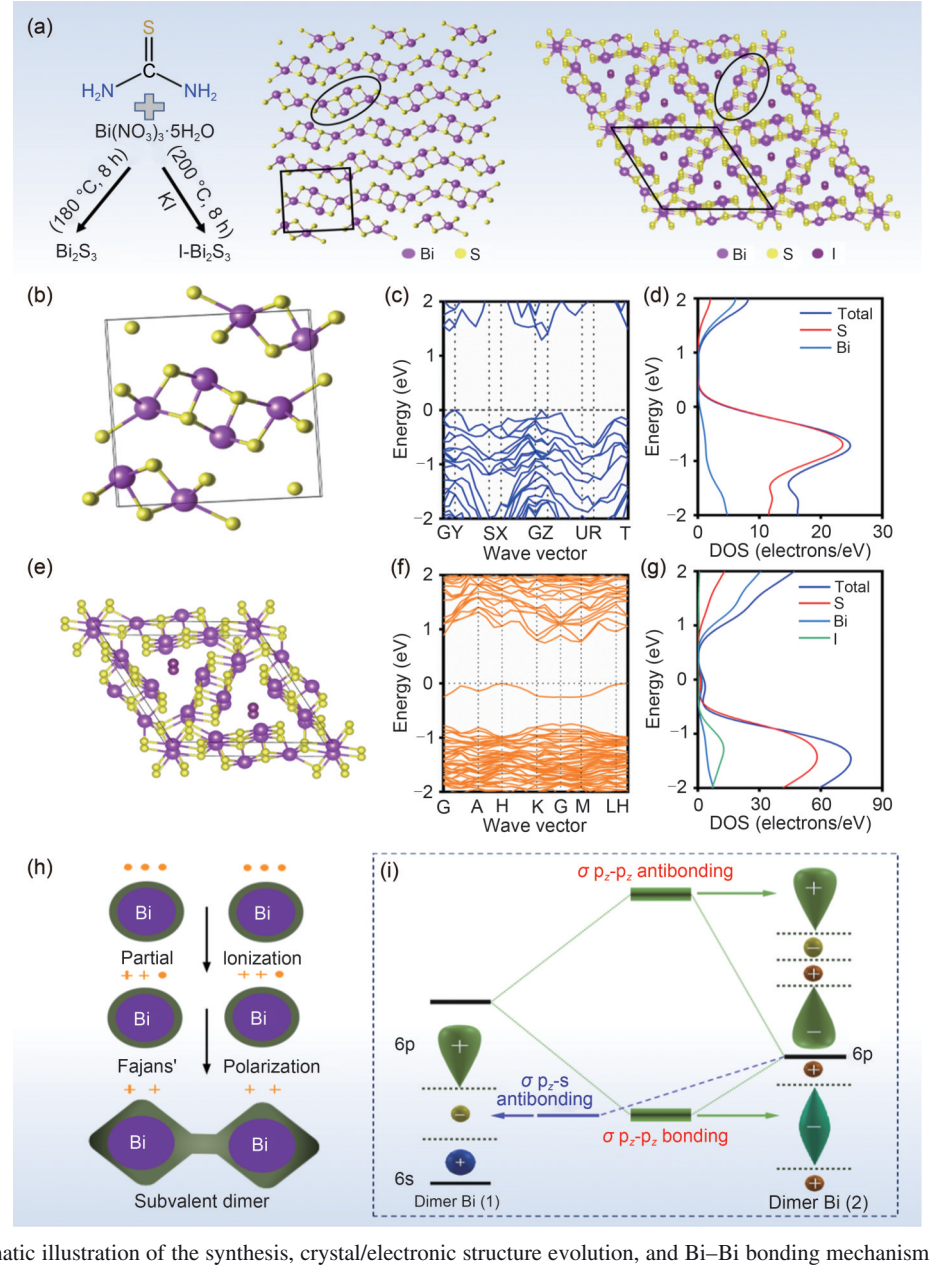

Fig. 2 Overall schematic illustration of the synthesis, crystal/electronic structure evolution, and Bi–Bi bonding mechanism in pristine Bi_2S_3 and iodine-modified I-Bi_2S_3. (a) Synthesis process of Bi_2S_3 and I-Bi_2S_3 (supercell structure diagram). (b, e) Crystal cell models of Bi_2S_3 (a= 11.941 506 Å, b=4.027 079 Å, c=11.164 037 Å) and I-Bi_2S_3. (c, d, f, g) Band structure and DOS of Bi_2S_3 and $Bi_{13}S_{18}I_2$ cells. (h) Formation diagram of bivalent Bi_2^{4+}. (i) Schematic of partial molecular orbital diagram for Bi–Bi dimer interaction involving $6p_z$ and 6s orbitals

0.333 33, 0.125 02). The distance between the two I atoms was 4.0168 Å.

Based on the DFT analysis, a new energy band curve appeared in the energy band structure of $Bi_{13}S_{18}I_2$ at the top of the VB, resulting in the narrowed bandgap of 0.746 eV. The TDOS and PDOS of Bi_2S_3 and $Bi_{13}S_{18}I_2$ were calculated to reveal the atomic orbital contributions to the band structure. In Figs. 2c, 2d, 2f, and 2g, the zero-energy level is attributed to the Fermi level. The TDOS curve of the $Bi_{13}S_{18}I_2$ crystal cell caused by iodine doping exhibits a bend near the Fermi level, which accounts for the emergence of a new energy level. The new energy level of the VB is dominated by S^{2-} and Bi_2^{4+} atoms (Fig. 2g). The formation diagram of bivalent Bi_2^{4+} is shown in Fig. 2h. To maintain the overall electroneutrality of the Bi_2S_3 crystal after iodine doping, two electrons from Bi $6p_x$ and $6p_y$ orbitals were ionized to compensate for the negative charge of I^- ions, resulting in the partial reduction of Bi^{3+} to Bi^{2+}. Subsequently, these Bi^{2+} species, located within star-shaped cage-like environments, preferentially formed covalent bonds with adjacent Bi^{2+} ions under Fajans' polarization, resulting in the formation of subvalent Bi_2^{4+} dimers. The

stability of the subvalent Bi_2^{4+} dimers in the $Bi_{13}S_{18}I_2$ unit cell can be attributed to the strong interaction between homonuclear Bi $6p_z$ orbitals with nearly perfect energy matching. This interaction resulted in the formation of bonding and antibonding molecular orbitals, with the Bi($6p_z$)–Bi($6p_z$) bonding states below the Fermi level stabilizing the Bi–Bi bond (Fig. 2i). Although Bi(6s)–Bi($6p_z$) antibonding caused slight weakening, the poor energy overlap was insufficient to overcome the overall bond stability. Therefore, the partial occupancy of Bi $6p_z$ orbitals confirms a Bi_2^{4+} subvalent state, supporting the $Bi_{13}S_{18}I_2$ stoichiometry in the P3 space group instead of that in $P6_3/m$, consistent with the XRD results.

Another possible explanation is that iodine doping induced a rearrangement of the initial Bi_2S_3 crystal cells with an orthorhombic space group (P*nma*), resulting in the formation of a new phase, $Bi_{19}(S_9I)_3$, with a hexagonal lattice ($P6_3/m$ space group). Specifically, in its primitive unit cell, three chain-like (Bi_4S_6) subunits are connected by two I atoms and two-thirds of a Bi atom, thereby forming a $Bi_{2/3}(Bi_4S_6)_3I_2$ unit with a narrow bandgap (0.85 eV): $Bi(Bi_2S_3)_9I_3$. In this case, as an indirect semiconductor, $Bi(Bi_2S_3)_9I_3$ can generate electron–hole pairs under NIR-II light excitation. Subsequently, the electrons and holes were relaxed to the band edges, ultimately releasing heat energy in the form of phonons (nonradiative decay process) [40]. In this study, the $Bi_{19}(S_9I)_3$ crystal structure was identified via the lattice fringes of the I-Bi_2S_3 powder (Fig. 1f). Therefore, the absorption wavelength of $(Bi_2S_3)_9I_3$ could be extended to the NIR-II region, thereby enhancing the photothermal effect via phonon scattering [41].

3.2 Electrical properties of I-Bi_2S_3 nanorods

Temperature variations can induce the movement of charge carriers (electrons and holes) in pyroelectric materials, directly converting thermal energy into electrical energy. To this end, the electrochemical properties of the I-Bi_2S_3 nanorods were analyzed using an electrochemical workstation and a UV-2700 spectrophotometer. The Mott–Schottky analysis revealed that the I-Bi_2S_3 nanorods are n-type semiconductors, as evidenced by the positive slope of the curve. The CB potential was determined to be −0.35 eV versus the standard calomel electrode (Fig. 3a). As shown in Figs. 3b and 3c, the bandgap widths of Bi_2S_3 and I-Bi_2S_3 were determined from their UV diffuse reflection absorption curves to be 1.23 and 0.88 eV, respectively, using the Tauc plot method [42]. The VB potentials of Bi_2S_3 and I-Bi_2S_3 were determined to be 0.88 and 0.53 eV, respectively, using the equation $E_{(VB)}=E_{(CB)}+E_g$ (Fig. 3d). These results reveal that I-Bi_2S_3 exhibits a relatively narrow bandgap, which is favorable for electron transition.

The charge transfer resistance of the samples was evaluated using EIS. The Nyquist plot of the I-Bi_2S_3 nanorod exhibited a markedly smaller semicircle radius than that of the Bi_2S_3 nanorod under 1064-nm laser irradiation (Fig. 3e), indicating its lower charge transfer resistance under the same temperature fluctuations [43]. To verify the influence of the material's optical properties on thermoelectric performance, the pyroelectric currents of Bi_2S_3 and I-Bi_2S_3 under 1064-nm laser radiation were measured (Fig. 3f). The I-Bi_2S_3 sample generated a stable average pyroelectric current of approximately 5 μA, which was significantly higher than that of the

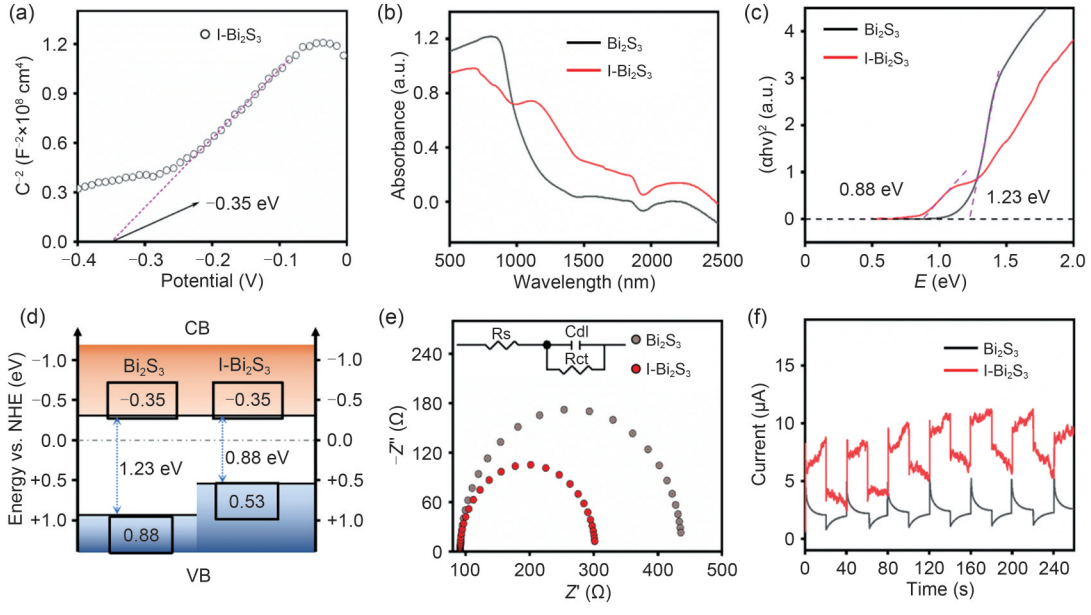

Fig. 3 Electrochemical analysis of I-Bi_2S_3. (a) Mott–Schottky curves of I-Bi_2S_3 nanorods. (b, c) UV–Vis/NIR diffuse reflection and bandgap of Bi_2S_3 and I-Bi_2S_3 nanorods. (d) Band structure distribution of Bi_2S_3 to I-Bi_2S_3. (e) EIS Nyquist plots of I-Bi_2S_3 nanorod treatment in the dark and under 1064-nm laser irradiation. (f) Pyroelectric current of Bi_2S_3 and I-Bi_2S_3 nanorods under 1064-nm laser-on/off irradiation

Bi_2S_3 sample. More importantly, the pyroelectric current for I-Bi_2S_3 exhibited good stability, whereas that of Bi_2S_3 only responded instantaneously and quickly disappeared. The results suggest that the electrons of I-Bi_2S_3 can be continuously excited to transition from the VB to the CB under energy input provided by 1064-nm laser irradiation [44]. In contrast, Bi_2S_3 with a wider bandgap requires a shorter-wavelength (higher-energy) light source to achieve sufficient excitation; thus, it fails to sustain a stable current. The difference in current (Fig. 3f) and absorption ability at different wavelength bands (Fig. 3b) confirms that the incorporation of iodine atoms reduces the bandgap of Bi_2S_3, thereby causing a red shift in the excitation wavelength [45].

In addition, the thermal conductivity (k) of the I-Bi_2S_3 nanorods at temperatures of 30 °C and 50 °C was investigated (Table 1). The thermal conductivity of I-Bi_2S_3 was significantly lower than that of pristine Bi_2S_3 across the measured temperature range. Specifically, the k value of I-Bi_2S_3 decreased to 0.041 W/(m·K) at 50 °C compared with the value of 0.044 W/(m·K) of Bi_2S_3. This pronounced reduction in k was primarily attributed to the dual low-energy vibration effect of I-Bi_2S_3, resulting from the localized vibrational modes introduced by iodine atoms and their interaction with Bi_2^{4+} atoms. The relatively heavy mass and weak bonding of iodine resulted in low-frequency rattling-like vibrations, which were coupled with the intrinsic low-energy modes of Bi_2^{4+} sites. This coupling intensified phonon scattering and disrupted heat transport through the lattice, thereby reducing the thermal conductivity.

Table 1 Thermal conductivity of samples

Temperature (°C)	Thermal conductivity k (W/(m·K))	
	Bi_2S_3	I-Bi_2S_3
30	0.043	0.040
50	0.044	0.041

3.3 Thermoelectric conversion ability of PLLA/I-Bi_2S_3 scaffold

This study aimed to prepare a tissue scaffold with excellent thermoelectric performance for tissue regeneration after tumor resection. As shown in Figs. 4a and 4b, the scaffold

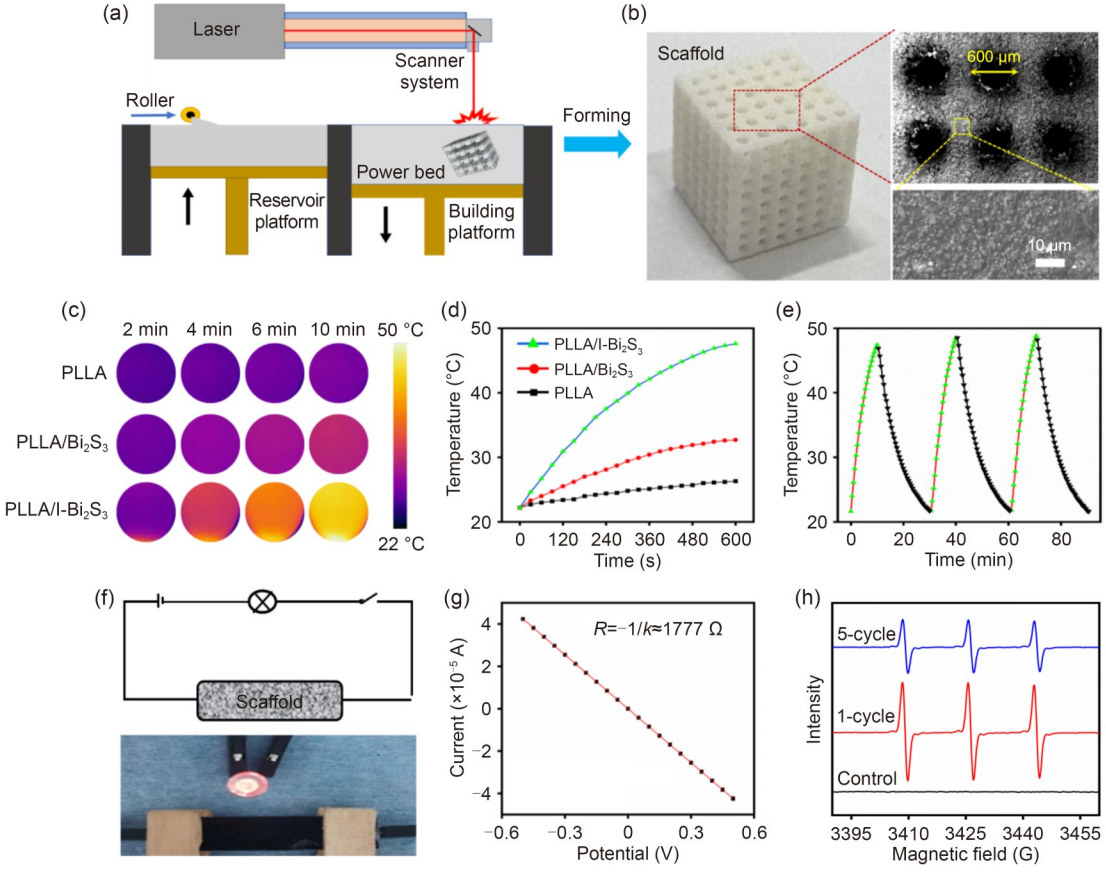

Fig. 4 Photothermal and thermoelectric performance of the scaffold. Preparation process (a) and microstructure (b) of the stent. Thermal imaging images (c) and temperature variation curves (d) of scaffolds under 1064-nm laser illumination. (e) Heating/Cooling curve of PLLA/I-Bi_2S_3 scaffold for three laser-on/off cycles. (f) Conductivity test of PLLA/I-Bi_2S_3 scaffold. (g) Resistance tests of the fitted PLLA/I-Bi_2S_3 scaffold. (h) ESR spectra demonstrating hot-electron generation of PLLA/I-Bi_2S_3 scaffold after one and five laser-on/off cycles

prepared by SLS technology possessed a complicated outline and a fine porous structure with an average pore size of 600 μm. In general, pore sizes of 200–800 μm promote cell adhesion, nutrient exchange, and vascularization, creating an ideal environment for tissue regeneration [46, 47]. The photothermal performance of all scaffolds was evaluated under 1064-nm laser irradiation, and the corresponding time–temperature curves were recorded. Based on the infrared thermography images, the immersion temperatures of all scaffolds, except for the PLLA group, increased with the extension of the illumination time (Fig. 4c). Notably, the immersion temperature of the PLLA/I-Bi_2S_3 group was significantly higher than that of the PLLA/Bi_2S_3 group under the same irradiation time. This result could be because I-Bi_2S_3 achieves stronger absorption and conversion at a wavelength of 1064 nm (Fig. 4d). Moreover, the temperature elevation of the PLLA/I-Bi_2S_3 group exhibited no significant decline after three heating/cooling cycles, demonstrating its good photothermal stability (Fig. 4e). In summary, the PLLA/I-Bi_2S_3 group exhibited relatively good photothermal efficiency compared with the PLLA/Bi_2S_3 group [48].

For thermoelectric scaffolds, good electrical conductivity is an important prerequisite for achieving thermoelectric functions [49]. To visually display the conductivity of the scaffolds, a light-emitting diode (LED) lighting test was conducted (Fig. 4f). The LED indicator successfully lit up after the PLLA/I-Bi_2S_3 scaffold was integrated into the series circuit, indicating that the I-Bi_2S_3 nanorod in the PLLA matrix formed a conductive network for current transmission [50]. In our previous work, we found that filled NPs could be distributed in the grain boundary of the polymer matrix due to the near-zero shearing action of the laser sintering process, thereby resulting in the formation of a connected network in the thermoelectric scaffold. Therefore, although the resistance of the PLLA/I-Bi_2S_3 scaffold reached 1777 Ω (Fig. 4g), it also achieved an internal conductivity function. The hot electrons released by the thermoelectric scaffold were detected using ESR under 1064-nm laser irradiation (Fig. 4h). Compared with the control group, the PLLA/I-Bi_2S_3 group exhibited obvious DMPO peaks after one cooling/heating cycle, confirming hot-electron generation. Furthermore, the intensities of these peaks significantly decreased after five cycles, indicating that the PLLA/I-Bi_2S_3 scaffold consumed the capture agents by continuously producing hot electrons [51].

Therefore, the thermoelectric conversion function of the thermoelectric scaffold can convert phototherapy heat into hot electrons, which can react with surrounding O_2 to generate ROS [52]. Therefore, the ability of the PLLA/I-Bi_2S_3 scaffold to generate ROS in vitro was examined via ESR. As shown in Figs. 5a and 5b, the PLLA/I-Bi_2S_3 scaffold could generate $^1O_2$ and ·OH under NIR-II laser irradiation, as evidenced by the 1:1:1 triplet characteristic signal of TEMP-$^1O_2$ and the 1:2:2:1 quadruple characteristic signal of the DMPO/·OH adduct. To investigate the positive effects after the introduction of I-Bi_2S_3 into the PLLA scaffold, the difference in ROS generation ability between the PLLA/Bi_2S_3 and PLLA/I-Bi_2S_3 scaffolds was explored using a fluorescence colorimetric method. In general, the absorption of DPBF at 416 nm decreases in the presence of $^1O_2$, whereas the absorption of TMB and OPD increases in the presence of ·OH. The DPBF peak intensity of the PLLA/I-Bi_2S_3 group was lower than that of the PLLA/Bi_2S_3 group under laser irradiation for 10 min (Fig. 5c), indicating that the incorporation of I-Bi_2S_3 enhanced the $^1O_2$ generation ability.

Similarly, the PLLA/I-Bi_2S_3 group exhibited a greater ·OH generation ability within the same laser irradiation duration than the PLLA/Bi_2S_3 group (Figs. 5d and 5e). Moreover, for the PLLA/I-Bi_2S_3 scaffold, the peak intensity of the DPBF solution continuously decreased with increasing number of heating/cooling cycles (Fig. 5f). This result indicates that the scaffold exhibits a stable thermoelectric effect under NIR-II laser irradiation [53]. These results confirm that the PLLA/I-Bi_2S_3 scaffold undergoes a light–heat–electric excitation process under NIR-II laser irradiation, ultimately generating desirable $^1O_2$ and ·OH radicals (Fig. 5g). In detail, the PLLA/I-Bi_2S_3 scaffold first generates a photothermal effect under NIR-II laser irradiation and then converts the temperature fluctuations of PTT into pyroelectric charges, which ultimately react with surrounding oxygen-containing substances to produce $^1O_2$ and ·OH. The ROS generation ability of the scaffold primarily originates from the thermoelectric effect, where a temperature gradient effectively drives charge separation and promotes electron transfer, thereby accelerating oxygen reduction. Notably, although photothermal effects can impair mitochondrial respiration and induce ROS generation under substantial hyperthermia, the mild photothermal heating observed in this study (<50 °C) is insufficient to markedly enhance ROS production.

3.4 In vitro antitumor properties of scaffolds

Osteosarcoma MG-63 cells were selected as receptor cells to experimentally evaluate the antitumor efficacy of the scaffolds. The fluorescence live/dead assay showed that the majority of MG-63 cells in the PLLA group were stained green (Fig. 6a), whereas those in the PLLA/Bi_2S_3 and PLLA/I-Bi_2S_3 groups appeared red, indicating that the composite scaffold exhibited good antitumor efficacy under NIR laser irradiation. Notably, the PLLA/I-Bi_2S_3 group exhibited a significantly higher number of dead cells than the PLLA/Bi_2S_3 group, highlighting its superior antitumor efficacy. In contrast, the majority of MG-63 cells in all scaffolds were dyed green in the absence of

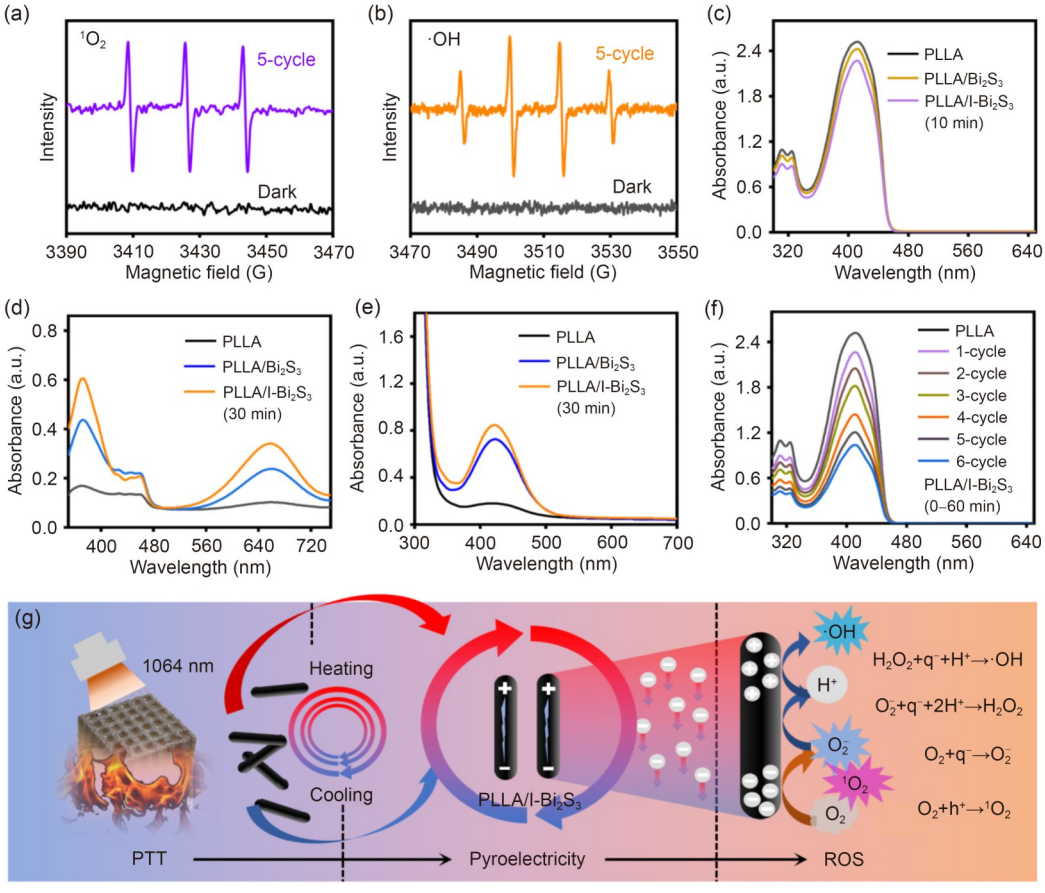

Fig. 5 Evaluation of ROS generation/release from the scaffold. ESR spectra demonstrating $^1O_2$ (a) and ·OH (b) generation after five laser-on/off cycles. (c) UV–Vis absorption spectra of DPBF after exposure of all scaffolds to 1064-nm laser irradiation. UV–Vis absorption spectra of TMB (d) and OPD (e) after exposure of PLLA/I-Bi_2S_3 scaffold to 1064-nm laser irradiation. (f) UV–Vis absorption spectra of DPBF after exposure of PLLA/I-Bi_2S_3 scaffold to multiple laser-on/off cycles. (g) Mechanism of energy conversion and ROS generation

laser irradiation (Fig. 6b), demonstrating their excellent biocompatibility [54].

Based on the optical density (OD) value changes of the CCK-8 assays (Fig. 6c), the tumor apoptosis rates under NIR laser irradiation were calculated as 64.5% and 84.6% for PLLA/Bi_2S_3 and PLLA/I-Bi_2S_3, respectively, whereas the rates without irradiation were only 1.8% and 1.1%, respectively (Fig. 6d). The cell adhesion tests further supported these findings, showing that cells adhered to the PLLA and PLLA/Bi_2S_3 scaffolds maintained relatively intact morphologies (Fig. 6e), whereas those on the PLLA/I-Bi_2S_3 scaffold were visibly ruptured, emphasizing its enhanced antitumor performance [55]. This conclusion was reinforced by nuclear staining (Fig. 6f), where fragmented nuclei were more obvious in the PLLA/Bi_2S_3 group than in the other two groups.

Furthermore, the ROS amounts in the tumor cells were examined, confirming that the PLLA/I-Bi_2S_3 scaffold produced more ROS under 1064-nm laser irradiation, as evidenced by the numerous green fluorescence peaks (Fig. 7a) and the increased quantitative ROS values (Fig. 7b). In contrast, in the absence of laser irradiation, the ROS amounts of all scaffolds were identical [56]. In general, HSPs in tumors are key factors that hinder the efficacy of PTT. Western blotting was used to assess HSP90 expression in MG-63 cells. The results demonstrated that the HSP90 expression in the PLLA group significantly increased after 1064-nm laser irradiation compared with that in the control group without laser exposure. The results demonstrated that HSP90 was rapidly activated in the heat-stress environment. The HSP90 expression in the PLLA/Bi_2S_3 scaffold was similar to that in the control group. In contrast, the HSP90 expression in the PLLA/I-Bi_2S_3 scaffold was significantly lower than that in the PLLA group, indicating that ROS produced by PLLA/I-Bi_2S_3 effectively suppressed HSP90 [57].

Tumor cell apoptosis and necrosis were examined using flow cytometry. The PLLA group exhibited relatively low apoptosis (Q3) and necrosis (Q2) levels, whereas the PLLA/Bi_2S_3 and PLLA/I-Bi_2S_3 groups exhibited markedly elevated apoptosis and necrosis levels under NIR-II laser irradiation (Fig. 7d). Based on the quantitative cell apoptosis

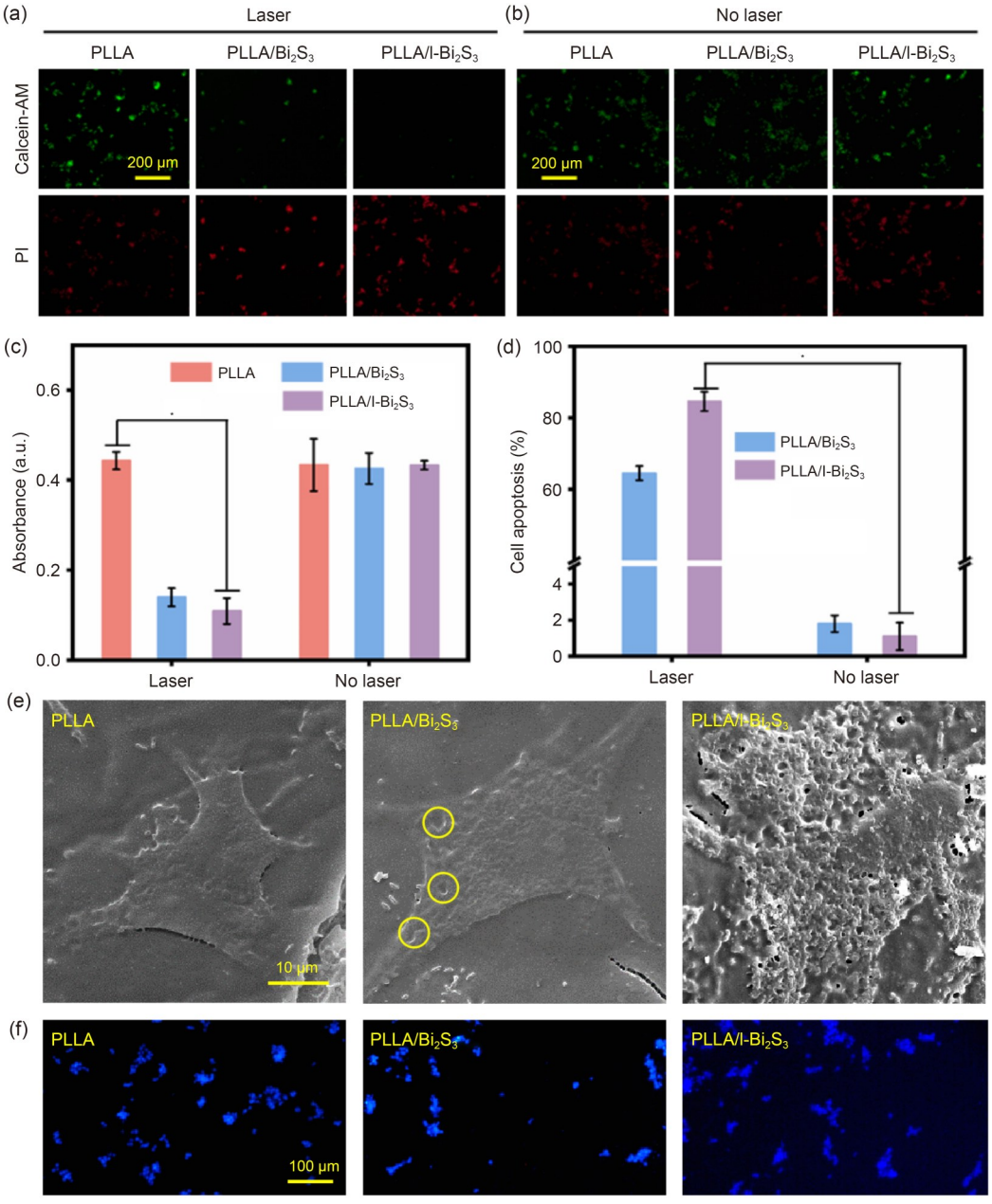

Fig. 6 In vitro antitumor evaluation of the scaffold. Fluorescence images of MG-63 cells under NIR-II laser (a) and without laser (b) exposure. CCK-8 results (c) and corresponding apoptosis rate (d). (e) SEM images of MG-63 cell adhesion. (f) Fluorescence images of cell nuclei in different scaffolds. The error bars indicate mean±standard deviation (n=5). $^{*}p \leq 0.05$

data (Fig. 7e), the PLLA/I-Bi_2S_3 scaffold exhibited excellent antitumor efficacy compared with the other two scaffold groups [58]. The antitumor mechanism of the scaffold is illustrated in Fig. 7f. After implantation, the scaffold gradually hydrolyzed and released I-Bi_2S_3 into the targeted lesion site. Upon NIR-II laser irradiation, the I-Bi_2S_3 nanorod generated localized heat via PTT, resulting in the thermal ablation of the tumor cells and increased membrane permeability. Simultaneously, the ROS produced by the thermoelectric effect disrupted HSPs, thereby weakening the tumor defense mechanisms and ultimately causing DNA damage and protein leakage. This innovative strategy integrates the precise release of I-Bi_2S_3 and ROS-mediated cell destruction and photothermal-induced ablation, maximizing therapeutic efficacy while minimizing collateral damage to healthy tissues.

3.5 Evaluation of in vivo antitumor ability of scaffolds

To further verify the antitumor performance of the scaffolds, in vivo animal experiments were conducted using a

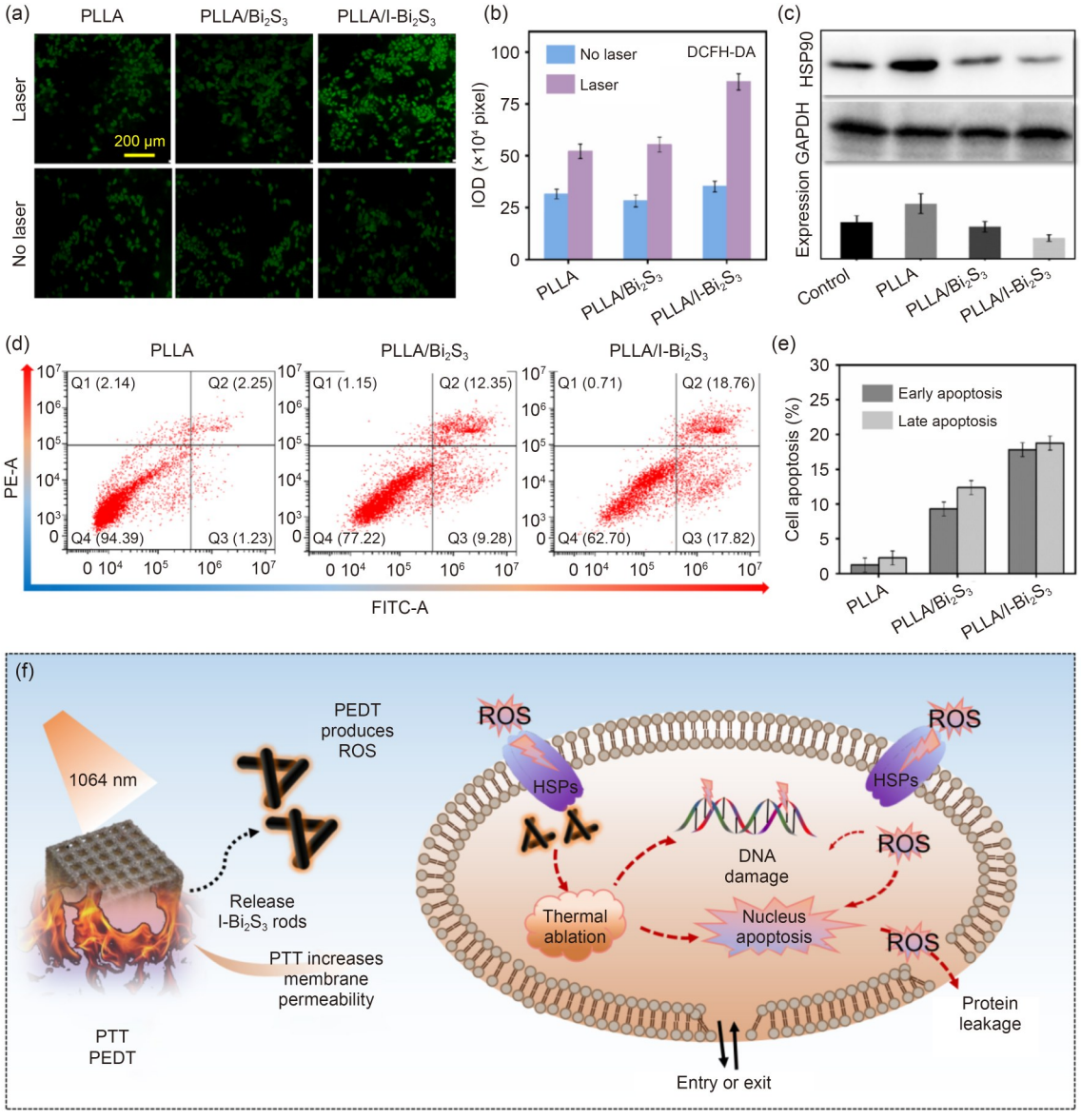

Fig. 7 Mechanistic analysis of scaffold antitumor activity. (a) Fluorescence microscopy images of ROS production. (b) Integrated OD value of fluorescence images of DCFH-DA. (c) Representative Western blotting and quantitative measurement of HSP90 expression. Flow cytometry (d) and relative statistics of tumor cell apoptosis (e). (f) Antitumor mechanism of the scaffold. The error bars indicate mean±standard deviation (n=5)

nude mouse model of orthotopic osteosarcoma (Fig. 8a). Different scaffolds were implanted into the dorsal region of the nude mice, followed by exposure to NIR-II laser irradiation (1064 nm, 1.5 W/cm^2, 9 min). According to the infrared thermal images, the temperature of the tumor sites for the PLLA/I-Bi_2S_3 group rapidly increased under NIR-II laser irradiation, reaching 42 °C in 3 min (Fig. 8b). In contrast, the PLLA/Bi_2S_3 group required a longer irradiation time to achieve the same temperature, which was consistent with the results of the in vitro photothermal experiments. Tumor volume changes were recorded after two weeks of cultivation (Fig. 8c). The tumor volume in the PLLA group increased over time, whereas the growth in the PLLA/Bi_2S_3 group was slower, indicating a slight tumor inhibition. In comparison, the tumor volume of the PLLA/I-Bi_2S_3 group was progressively reduced over time, indicating its superior antitumor efficacy.

Fourteen days after surgery, the nude mice were euthanized, and tumor tissues were collected from each group for further evaluation of necrosis and apoptosis using section staining techniques. The photothermal photographs of the tumors excised from the wound sites are shown in Fig. 8d. The tumor size in the PLLA/I-Bi_2S_3 group was significantly smaller than that in the other two groups, demonstrating its superior efficacy in eliminating tumor cells. Tumor necrosis and apoptosis were assessed using H&E staining and

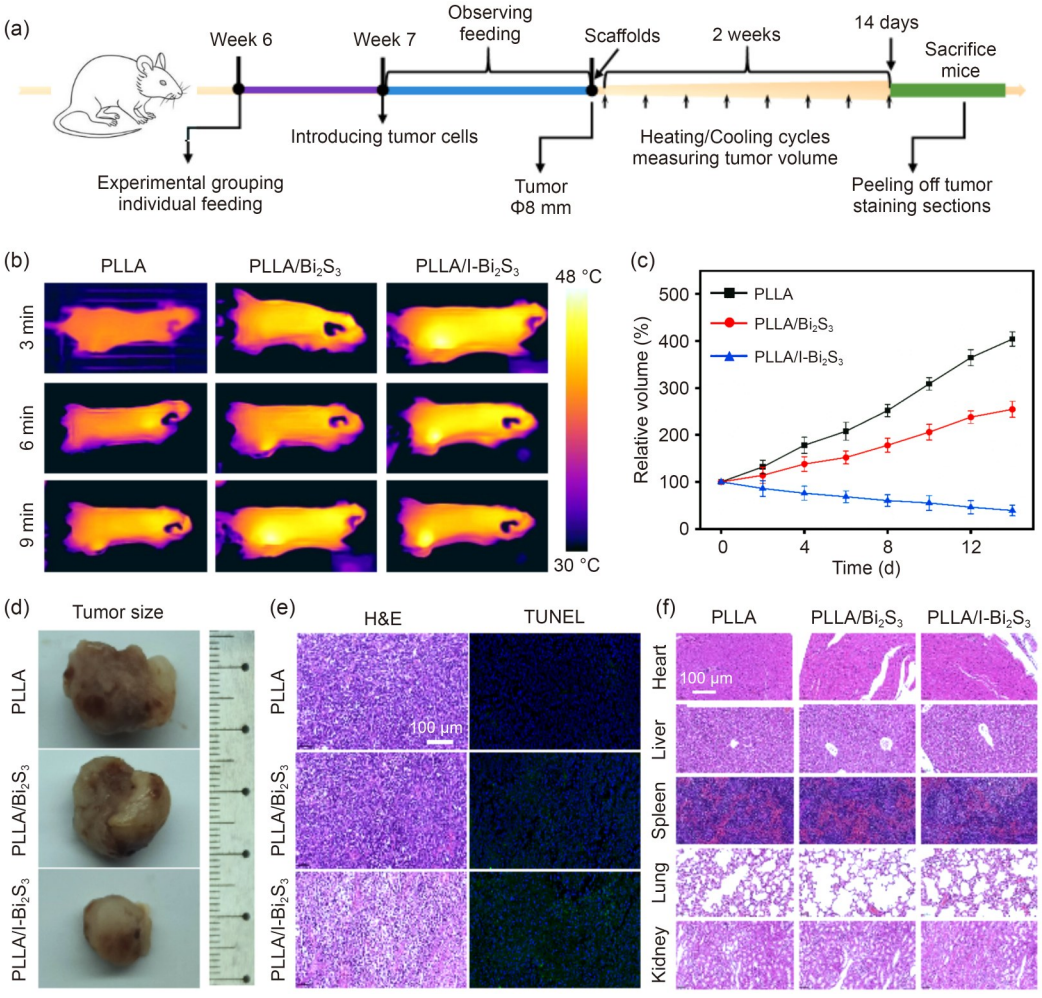

Fig. 8 In vivo antitumor assay of scaffolds. (a) Experimental procedure for tumor treatment in nude mice. (b) Photothermal imaging of nude mice under 1064-nm laser irradiation for 9 min at 1.5 W/cm^2. (c) Tumor volume changes over time. (d) Weight of isolated tumors for different scaffolds. (e) Representative images of H&E and TUNEL staining in tumor tissues. (f) H&E staining of pathological sections from major organs (heart, liver, spleen, lung, and kidney) of nude mice treated with scaffolds. The error bars indicate mean±standard deviation (n=3)

TUNEL staining, respectively. The H&E staining results revealed no significant differences in nuclear staining between the PLLA/Bi_2S_3 and PLLA groups (Fig. 8e). In contrast, the PLLA/I-Bi_2S_3 group exhibited a markedly reduced presence of cells with blue/purple staining (nuclei), indicating its higher level of necrotic osteosarcoma cells.

Similarly, the TUNEL staining results revealed a larger number and more extensive areas of green-stained apoptotic tumor cells in the PLLA/I-Bi_2S_3 group than in the other two groups. These results confirm the superior capacity of the PLLA/I-Bi_2S_3 group to induce apoptosis in tumor cells [59]. Moreover, the in vivo biocompatibility of the scaffolds was evaluated by staining the key organs (heart, liver, spleen, lungs, and kidneys) of each nude mouse (Fig. 8f) [60]. The results revealed no significant inflammatory or physiological damage to any organ, indicating that all scaffolds exhibited good biocompatibility and biosafety.

4 Conclusions

In this study, a novel antitumor PLLA/I-Bi_2S_3 scaffold was synthesized based on photothermal–thermoelectric therapy, providing a promising therapeutic solution for tissue regeneration following osteosarcoma resection. The key findings are as follows:

(1) Bi_2S_3 nanorods with excellent photothermal–thermoelectric functions were synthesized using a hydrothermal reaction method. Iodine doping significantly enhanced the thermoelectric efficiency while broadening the light absorption range to the NIR-II region, thereby enabling effective deep tissue therapy.

(2) Synthesized I-Bi_2S_3 nanorods were integrated into the PLLA matrix using SLS technology, aiming to fabricate a dual-function antitumor scaffold. Under NIR-II laser irradiation, the scaffolds achieved a light–heat–electric conversion process, facilitating localized tumor ablation via photothermal

effects and ROS generation via thermoelectric effects. The scaffolds exhibited an antitumor rate of 84.6% against osteosarcoma cells, demonstrating their superior antitumor performance.

(3) Upon implantation, the scaffold gradually hydrolyzed, releasing I-Bi_2S_3 NPs precisely at the lesion sites. This controlled release minimized collateral damage to healthy tissues while maximizing therapeutic efficacy. In vivo experiments confirmed that the scaffold caused no adverse effects on major organs (heart, liver, spleen, lungs, and kidneys), ensuring its biocompatibility and safety.

Acknowledgements This study was supported by the following funds: (1) National Key Research and Development Program of China (No. 2023YFB4605800); (2) The National Natural Science Foundation of China (Nos. 52475362, 52365046, and 52465041); (3) Jiangxi Provincial Natural Science Foundation of China (No. 20224ACB204013); (4) Jiangxi Provincial Key Laboratory of Additive Manufacturing of Implantable Medical Device (No. 2024SSY11161); (5) Jiangxi Provincial Department of Education Science and Technology Project (No. GJJ2400708); (6) Jiangxi Province Science and Technology Program (Nos. 20252BAC200317 and 20252BEJ730195).

Author contributions JZ (Jun Zan) and JCZ participated in conceptualization, validation, methodology, formal analysis, investigation, and writing of the original draft. JZ (Jie Zeng) was involved in methodology and validation. QY was involved in cell experiment analysis. HYY was involved in supervision, conceptualization, and funding acquisition. YWY and CJS were involved in conceptualization, funding acquisition, supervision, and writing—review & editing.

Declarations

Conflict of interest CJS is an associate editor of *Bio-Design and Manufacturing* and was not involved in the editorial review or the decision to publish this article. The authors declare that they have no known competing financial interests or personal relationships that could have appeared to influence the work reported in this paper.

Ethical approval All animal experiments were approved by the Research Ethics Committee of the Third Xiangya Hospital of Central South University (Approval No. XMSB-2023-0164).

Data availability The datasets generated and/or analyzed during this study are available from the corresponding authors upon reasonable request.

Use of generative AI tools No generative AI tools were used in the preparation of this manuscript.

References

1. Lee JA, Lim J, Jin HY et al (2021) Osteosarcoma in adolescents and young adults. *Cells* 10(10):2684. https://doi.org/10.3390/cells10102684
2. Lee H, Han G, Na Y et al (2024) 3D-printed tissue-specific nanospike-based adhesive materials for time-regulated synergistic tumor therapy and tissue regeneration in vivo. *Adv Funct Mater* 34(48):2470281. https://doi.org/10.1002/adfm.202470281
3. Parmeggiani A, Miceli M, Errani C et al (2021) State of the art and new concepts in giant cell tumor of bone: imaging features and tumor characteristics. *Cancers* 13(24):6298. https://doi.org/10.3390/cancers13246298
4. Wang Y, Zhang HY, Qiang HF et al (2024) Innovative biomaterials for bone tumor treatment and regeneration: tackling postoperative challenges and charting the path forward. *Adv Healthc Mater* 13(16):2304060. https://doi.org/10.1002/adhm.202304060
5. Huang WJ, Cheng S, Wang XL et al (2021) Noncompressible hemostasis and bone regeneration induced by an absorbable bioadhesive self-healing hydrogel. *Adv Funct Mater* 31(22): 2009189. https://doi.org/10.1002/adfm.202009189
6. Wang YH, Sun L, Mei ZG et al (2020) 3D printed biodegradable implants as an individualized drug delivery system for local chemotherapy of osteosarcoma. *Mater Des* 186:108336. https://doi.org/10.1016/j.matdes.2019.108336
7. Yang WJ, Zhou CY, He CX et al (2025) Defect engineering synergistically boosts the catalytic activity of Fe-MoO_v for highly efficient breast mesh antitumor therapy. *J Colloid Interface Sci* 678:260–271. https://doi.org/10.1016/j.jcis.2024.08.195
8. Ansari MAA, Golebiowska AA, Dash M et al (2022) Engineering biomaterials to 3D-print scaffolds for bone regeneration: practical and theoretical consideration. *Biomater Sci* 10(11): 2789–2816. https://doi.org/10.1039/d2bm00035k
9. Shuai CJ, Zhao Y, Deng YW et al (2024) Heterogeneous grain structure in biodegradable Zn prepared via mechanical alloying and laser powder bed fusion for strength-plasticity synergy. *Virtual Phys Prototyp* 19(1):e2317780. https://doi.org/10.1080/17452759.2024.2317780
10. Lee H, Shin DY, Na Y et al (2023) Antibacterial PLA/Mg composite with enhanced mechanical and biological performance for biodegradable orthopedic implants. *Biomater Adv* 152:213523. https://doi.org/10.1016/j.bioadv.2023.213523
11. Yuan JP, Ye ZY, Zeng YX et al (2022) Bifunctional scaffolds for tumor therapy and bone regeneration: synergistic effect and interplay between therapeutic agents and scaffold materials. *Mater Today Bio* 15:100318. https://doi.org/10.1016/j.mtbio.2022.100318
12. Guan HY, Zou PJ, Lin R et al (2023) Implantable self-powered therapeutic pellet for wireless photodynamic/sonodynamic hybrid therapy of cancer recurrence inhibition and tumor regression. *Nano Energy* 105:108002. https://doi.org/10.1016/j.nanoen.2022.108002
13. Mustapha A, Ismail A, Abdullahi SU et al (2021) Cancer chemotherapy: a review update of the mechanisms of actions, prospects and associated problems. *BIOMED Nat Appl Sci* 1(1): 1–19. https://doi.org/10.53858/bnas01010119
14. Shuai CJ, Xu WT, He HF et al (2024) Layered co-continuous structure in bone scaffold fabricated by laser additive manufacturing for enhancing electro-responsive shape memory properties. *J Mater Res Technol* 30:61–69. https://doi.org/10.1016/j.jmrt.2024.03.050
15. Nasseri B, Alizadeh E, Bani F et al (2022) Nanomaterials for photothermal and photodynamic cancer therapy. *Appl Phys Rev* 9:011317. https://doi.org/10.1063/5.0047672
16. Premji TP, Dash BS, Das S et al (2024) Functionalized nanomaterials for inhibiting ATP-dependent heat shock proteins in cancer photothermal/photodynamic therapy and combination therapy. *Nanomaterials* 14(1):112.

https://doi.org/10.3390/nano14010112
17. Di YF, Deng RZ, Liu Z et al (2023) Optimized strategies of ROS-based nanodynamic therapies for tumor theranostics. *Biomaterials* 303:122391. https://doi.org/10.1016/j.biomaterials.2023.122391
18. Zang PY, Du YQ, Yu CH et al (2023) Photothermal-actuated thermoelectric therapy by harnessing Janus-structured Ag–Ag_2S nanoparticles with enhanced antitumor efficacy. *Chem Mater* 35(18):7770–7780. https://doi.org/10.1021/acs.chemmater.3c01637
19. Wang Q, Du J, Ouyang RZ et al (2023) Recent advances in functional bismuth chalcogenide nanomaterials: cancer theranostics, antibacterial and biosensing. *Coord Chem Rev* 492: 215281. https://doi.org/10.1016/j.ccr.2023.215281
20. Theja VCS, Karthikeyan V, Musah JD et al (2022) Thermoelectric properties of sulfide and selenide-based materials. In: Dalapati G, Wong TS, Kundu S et al (Eds.), Sulfide and Selenide Based Materials for Emerging Applications. Elsevier, Amsterdam, the Netherlands, p.293–328. https://doi.org/10.1016/b978-0-323-99860-4.00009-5
21. Shankar MR, Prabhu AN (2023) A review on structural characteristics and thermoelectric properties of mid-temperature range chalcogenide-based thermoelectric materials. *J Mater Sci* 58(43): 16591–16633. https://doi.org/10.1007/s10853-023-09028-8
22. Guo J, Lou Q, Qiu Y et al (2020) Remarkably enhanced thermoelectric properties of Bi_2S_3 nanocomposites via modulation doping and grain boundary engineering. *Appl Surf Sci* 520:146341. https://doi.org/10.1016/j.apsusc.2020.146341
23. Ai LL, Jia DZ, Guo NN et al (2020) Cl-doped Bi_2S_3 homojunction nanorods with rich-defects for collaboratively boosting photocatalytic reduction performance. *Appl Surf Sci* 529:147002. https://doi.org/10.1016/j.apsusc.2020.147002
24. Chang XQ, Zhong JX, Yang G et al (2023) Targeted passivation and optimized interfacial carrier dynamics improving the efficiency and stability of hole transport layer-free narrow-bandgap perovskite solar cells. *Sci Bull* 68(12):1271–1282. https://doi.org/10.1016/j.scib.2023.05.012
25. Ran YJ, Ma WX, Yu HL et al (2024) Enhanced thermoelectric performance of $Mg_3Sb_{2-x}Bi_x$ thermoelectric thin films through carrier concentration modulation by Bi alloying. *J Alloys Compd* 985:174028. https://doi.org/10.1016/j.jallcom.2024.174028
26. Ye WP, Wang S, Hou XW et al (2023) Construction of Bi_2S_3/rGO heterointerfaces for enhanced and tunetable electromagnetic wave absorption. *Compos Commun* 37:101433. https://doi.org/10.1016/j.coco.2022.101433
27. Meng NQ, Xu PJ, Wen CC et al (2023) Near-infrared-II-activatable sulfur-deficient plasmonic Bi_2S_{3-x}-Au heterostructures for photoacoustic imaging-guided ultrasound enhanced high performance phototherapy. *J Colloid Interface Sci* 644: 437–453. https://doi.org/10.1016/j.jcis.2023.04.108
28. Yao X, Li DS, Gao CD et al (2024) Magnetostrictive strain-sensitivity synergy for laser-beam powder bed fusion processed $Fe_{81}Ga_{19}$ alloys by magnetic field annealing. *Adv Powder Mater* 3(5):100216. https://doi.org/10.1016/j.apmate.2024.100216
29. Yang WJ, Tong QY, He CX et al (2024) Mechanically propelled ion exchange regulates metal/bioceramic interface characteristics to improve the corrosion resistance of Mg composite for orthopedic applications. *Ceram Int* 50(13):23124–23134. https://doi.org/10.1016/j.ceramint.2024.04.036
30. Perdew J, Burke K, Ernzerhof M (1996) Generalized gradient approximation made simple. *Phys Rev Lett* 77(18):3865–3868. https://doi.org/10.1103/PhysRevLett.77.3865
31. Nkwe VM, Olatunde OC, Ben Smida Y et al (2023) Synthesis, characterization, computational studies, and photocatalytic properties of Cu doped Bi_2S_3 nanorods. *Mater Today Commun* 34: 105418. https://doi.org/10.1016/j.mtcomm.2023.105418
32. Abolade SA, Akinpelu SB, Obada DO et al (2024) Insights into the band gap anomalies of certain bismuth-based chalcogenides through ab initio calculations of structural and electronic properties. *Results Phys* 64:107891. https://doi.org/10.1016/j.rinp.2024.107891
33. Bai J, Shen S, Liu Y et al (2025) Magnesium and gallium-coloaded microspheres accelerate bone repair via osteogenesis and antibiosis. *Bio-Des Manuf* 8(1):150–165. https://doi.org/10.1631/bdm.2300253
34. Di W, Yan ZY, Shuai CJ et al (2024) A chemotherapy-photothermal synergistic system in bifunctional bone scaffold: tumor therapy and bone repair. *Mater Des* 245:113269. https://doi.org/10.1016/j.matdes.2024.113269
35. Xiong JS, Bian QH, Lei SJ et al (2021) $Bi_{19}S_{27}I_3$ nanorods: a new candidate for photothermal therapy in the first and second biological near-infrared windows. *Nanoscale* 13(10):5369–5382. https://doi.org/10.1039/d0nr09137e
36. Li S, Xu LF, Kong XG et al (2021) $Bi_{13}S_{18}X_2$-based solar cells (X=Cl, Br, I): photoelectric behavior and photovoltaic performance. *Phys Rev Applied* 15(3):034040. https://doi.org/10.1103/physrevapplied.15.034040
37. Peng SL, Li HJ, Zhang CY et al (2022) Promoted mid-infrared photodetection of PbSe film by iodine sensitization based on chemical bath deposition. *Nanomaterials* 12(9):1391. https://doi.org/10.3390/nano12091391
38. Groom RA, Jacobs A, Cepeda M et al (2017) Structural and optical properties of Sb-substituted BiSI grown from sulfur/iodine flux. *Inorg Chem* 56(20):12362–12368. https://doi.org/10.1021/acs.inorgchem.7b01839
39. Groom R, Jacobs A, Cepeda M et al (2017) $Bi_{13}S_{18}I_2$: (Re)discovery of a subvalent bismuth compound featuring $[Bi_2]^{4+}$ dimers grown in sulfur/iodine flux mixtures. *Chem Mater* 29(7):3314–3323. https://doi.org/10.1021/acs.chemmater.7b00702
40. Kurian A, Sumathi S (2024) Photocatalytic degradation of organic pollutants using heterojunction nanocomposite based on bismuth compound. In: Sathishkumar P (Ed.), Photocatalysis for Energy and Environmental Applications. Springer Nature, Singapore, p.229–254. https://doi.org/10.1007/978-981-97-1939-6_7
41. Guo J, Chen L, Wu Y et al (2020) Facile synthesis of N-type hexagonal $(Bi(Bi_2S_3)_9)I_3)_{0.667}$ as a promising thermoelectric compound. *Chem Commun* 56(79:11839–11842. https://doi.org/10.1039/d0cc05144f
42. Tauc J, Grigorovici R, Vancu A (1966) Optical properties and electronic structure of amorphous germanium. *Phys Status Solidi B* 15(2):627–637. https://doi.org/10.1002/pssb.19660150224
43. Zhang S, Wu LN, Shi WQ et al (2023) Nanoheterojunction engineering enables NIR-II-triggered photonic hyperthermia and pyroelectric catalysis for tumor-synergistic therapy. *Adv Funct Mater* 33(29):2302360. https://doi.org/10.1002/adfm.202302360
44. Bin C, Wang JH, Fan LL et al (2020) Visible light responsive Bi_2S_3-graphene/TiO_2 nanocomposites: one pot-hydrothermal synthesize and improved photocatalytic properties. *Fuller Nanotub Carbon Nanostruct* 28(6):500–508. https://doi.org/10.1080/1536383X.2020.1711516

45. Wang WN, Pei P, Chu ZY et al (2020) Bi_2S_3 coated Au nanorods for enhanced photodynamic and photothermal antibacterial activities under NIR light. *Chem Eng J* 397:125488. https://doi.org/10.1016/j.cej.2020.125488
46. Mohammadi H, Sepantafar M, Muhamad N et al (2021) How does scaffold porosity conduct bone tissue regeneration? *Adv Eng Mater* 23(10):2100463. https://doi.org/10.1002/adem.202100463
47. Zhao DW, Liu BY, Wang F et al (2025) Research and clinical applications of selective laser melting tantalum bone plates. *Bio-Des Manuf* 8(1):134–149. https://doi.org/10.1631/bdm.2300321
48. Zhang CY, Li DD, Pei P et al (2020) Rod-based urchin-like hollow microspheres of Bi_2S_3: facile synthesis, photo-controlled drug release for photoacoustic imaging and chemo-photothermal therapy of tumor ablation. *Biomaterials* 237:119835. https://doi.org/10.1016/j.biomaterials.2020.119835
49. Qi FW, Liao RB, Shuai Y et al (2022) A conductive network enhances nerve cell response. *Addit Manuf* 52:102694. https://doi.org/10.1016/j.addma.2022.102694
50. Huang YZ, Wang YQ, Fu Y (2022) 3D hierarchical biobased gel electrolyte with superior ionic conductivity and flame resistance for suppressing lithium dendrites via alloying and sieving mechanisms. *Compos Part B Eng* 230:109501. https://doi.org/10.1016/j.compositesb.2021.109501
51. Yang ZF, Xia XN, Yang WW et al (2021) Photothermal effect and continuous hot electrons injection synergistically induced enhanced molecular oxygen activation for efficient selective oxidation of benzyl alcohol over plasmonic $W_{18}O_{49}/ZnIn_2S_4$ photocatalyst. *Appl Catal B Environ* 299:120675. https://doi.org/10.1016/j.apcatb.2021.120675
52. Kang Y, Kong N, Ou MT et al (2023) A novel cascaded energy conversion system inducing efficient and precise cancer therapy. *Bioact Mater* 20:663–676. https://doi.org/10.1016/j.bioactmat.2022.07.007
53. Wang LL, Fu Y, Li QC et al (2022) EPR evidence for mechanistic diversity of Cu(II)/peroxygen oxidation systems by tracing the origin of DMPO spin adducts. *Environ Sci Technol* 56(12): 8796–8806
54. Colak B, Ertas YN (2024) Implantable, 3D-printed alginate scaffolds with bismuth sulfide nanoparticles for the treatment of local breast cancer via enhanced radiotherapy. *ACS Appl Mater Interfaces* 16(13):15718–15729. https://doi.org/10.1021/acsami.3c17024
55. Zhang WH, Chen Y, Li MY et al (2023) A PDA-functionalized 3D lung scaffold bioplatform to construct complicated breast tumor microenvironment for anticancer drug screening and immunotherapy. *Adv Sci* 10(26):2302855. https://doi.org/10.1002/advs.202302855
56. Qi FW, Liu W, Li ZK et al (2024) Reactive oxygen species responsive nitric oxide release for enhanced photodynamic antibacterial therapy of scaffolds. *ACS Appl Polym Mater* 6(11): 6581–6593. https://doi.org/10.1021/acsapm.4c00861
57. Liu KY, Zhang L, Lu HL et al (2023) Enhanced mild-temperature photothermal therapy by pyroptosis-boosted ATP deprivation with biodegradable nanoformulation. *J Nanobiotechnol* 21(1):64. https://doi.org/10.1186/s12951-023-01818-1
58. Van der Meeren L, Verduijn J, Krysko DV et al (2023) High-throughput mechano-cytometry as a method to detect apoptosis, necroptosis, and ferroptosis. *Cell Prolif* 56(6):e13445. https://doi.org/10.1111/cpr.13445
59. Liu YM, Zhang FY, Sun Q et al (2023) Adalimumab combined with erythropoietin improves recovery from spinal cord injury by suppressing microglial M1 polarization-mediated neural inflammation and apoptosis. *Inflammopharmacology* 31(2): 887–897. https://doi.org/10.1007/s10787-022-01090-z
60. Olugbodi JO, Lawal B, Bako G et al (2023) Effect of subdermal exposure of silver nanoparticles on hepatic, renal and cardiac functions accompanying oxidative damage in male Wistar rats. *Sci Rep* 13:10539. https://doi.org/10.1038/s41598-023-37178-x